Full Spherical High Dynamic Range Imaging from the Sky

Fumio Okura, Masayuki Kanbara, Naokazu Yokoya
Graduate School of Information Science
Nara Institute of Science and Technology (NAIST)
Nara, Japan
Email: {*fumio-o,kanbara,yokoya*}*@is.naist.jp*

Abstract—This paper describes a method for acquiring full spherical high dynamic range (HDR) images with no missing areas by using two omnidirectional cameras mounted on the top and bottom of an unmanned airship. The full spherical HDR images are generated by combining multiple omnidirectional images that are captured with different shutter speeds. The images generated are intended for uses in telepresence, augmented telepresence, and image-based lighting.

Keywords-omnidirectional camera; high dynamic range; telepresence; augmented telepresence; image based lighting

I. INTRODUCTION

This paper proposes an aerial imaging system that can capture full spherical images without missing areas and with high dynamic range (HDR) for telepresence [1], image-based lighting (IBL) [2], and augmented telepresence [3]. It should be noted that a full spherical image means an image covering the $360° \times 360°$ field of view of a full sphere. Telepresence is a technology providing a user with a view of a remote site with high immersiveness and is one of the major research fields in virtual reality. In particular, offline telepresence uses preliminarily recorded spherical (omnidirectional) images to provide users with views in any direction from a location and has become very important with the popularization of walk-through applications such as Google Street View [4]. Recently, there have been studies dealing with augmented telepresence [3], which provides the user with both the view of a remote site and related information by using augmented reality (AR) techniques [5]. The augmented telepresence system [3] not only realizes offline telepresence using recorded aerial spherical images but also renders CG models of buildings with IBL, which is a high-quality lighting technique using spherical images as environmental light maps [2].

This paper proposes an aerial imaging system to resolve two problems when spherical images are observed by omnidirectional cameras for telepresence, IBL, and augmented telepresence: 1) **occurrence of missing areas**, and 2) **deficiency of dynamic range**. In the rest of this paper, each problem and the related works are specified, and the approaches that we employed are described.
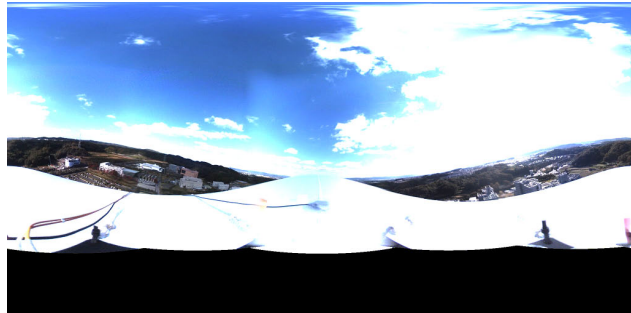
(a) Image captured from top of airship
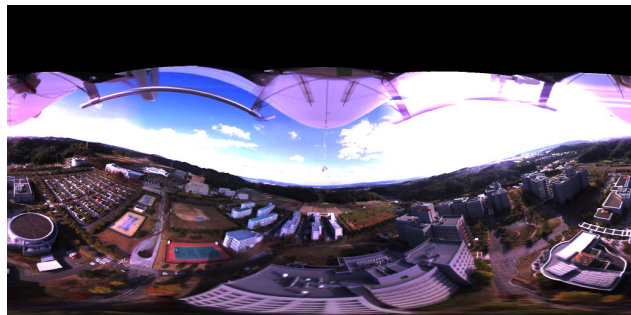
(b) Image captured from bottom of airship
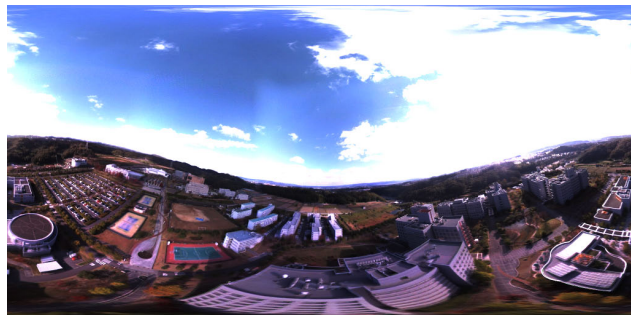
(c) Full spherical image

Figure 1. Full spherical HDR image generated from multi-exposure images captured by two omnidirectional cameras visualized with same exposure.

II. PROBLEMS AND RELATED WORKS

A. Occurrence of missing areas

Missing areas sometimes appear in a spherical image as shown in Figs. 1(a) and 1(b). These areas are caused by the

restriction of the field of view of the omnidirectional camera and (in the case of Fig. 1) by occlusions from the airship. Such areas decrease the immersiveness in telepresence and make it impossible to use the spherical images for IBL.

The approaches to fill the missing areas are divided into two categories as follows:

1) **Approaches not using observed intensities.** A previous work on augmented telepresence [3] filled a missing area in the upper hemisphere of spherical videos by using a sky model that represents a statistical model of various weather conditions. Another work using image inpainting techniques [6] filled the missing areas from the image itself. These are categorized as approaches not using observed intensities of missing areas such as with a model-based approach.

2) **Approaches using observed intensities.** Kawai et al. [7] treated a missing area in the ground portion of spherical video sequences captured in motion. The intensities of the missing area were estimated from the intensities of the images that observed the same place from other viewpoints. This is categorized as one approach using observed intensities of missing areas.

The former category of approach does not aim to estimate the real intensities in the missing areas but aims to fill the missing areas to decrease the strange appearance. The intensities estimated by the approach may have great differences from the real intensities. This is a cause of great differences in shade or shadow between real and virtual objects in IBL. Hence, this study applies the latter category of approach, by which the real intensities can be observed. In this study, two omnidirectional cameras mounted on the top and bottom of an unmanned airship capture the whole scene as shown in Fig. 1(c).

B. Deficiency of dynamic range

Spherical images without saturation of intensity are recommended for IBL [8]. However, the dynamic range of outdoor scenes is too high to capture using standard cameras that have normal (8-bit) dynamic range, as the sun can be 2^{17} times brighter than the dark areas in the clouds or the sky [9]. An HDR imaging method using low dynamic range (LDR) images captured with multiple exposure values (multi-exposure images), as proposed by Debevec and Malik [8], is widely used to capture a scene by means of LDR cameras without saturation. We employ this method to generate spherical HDR images.

When the images are captured in motion, misalignment appears among the multi-exposure images. Although there have been some studies to overcome this problem [10], it remains difficult to correct a large misalignment. It is better to apply fewer exposure values in the case that camera velocity and frame rate are constant. In this study, to generate HDR images effectively from a small number of multi-exposure images, shutter speeds are controlled automatically using an
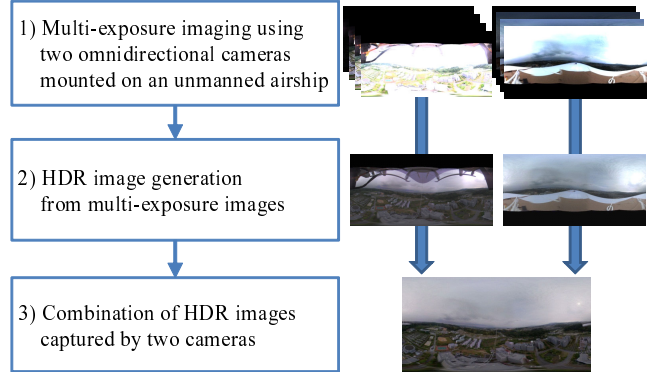

Figure 2. Flow of proposed aerial imaging. Right images are examples of output of each process.

HDR histogram generated from previously captured images. An omnidirectional camera mounted atop the vehicle mainly captures the sun and sky, which are too bright to capture without saturation even if the highest shutter speed is used. Neutral density (ND) filters are attached to the camera to overcome the problem as was done in related work [9] that directly captured the sun and sky.

In this paper, the process of the proposed system is divided into three parts: 1) multi-exposure imaging using two omnidirectional cameras mounted on an unmanned airship, 2) HDR image generation from multi-exposure images, and 3) combination of HDR images captured by two cameras. This paper also shows experimental results of generating full spherical HDR images using aerial image sequences.

III. FULL SPHERICAL HDR IMAGING

A. Overview

The proposed system generates full spherical images using multi-exposure images captured with two omnidirectional cameras mounted on the top and bottom of an unmanned airship. The process of the proposed system is divided into three parts as shown in Fig. 2. Each part is described in detail in the following paragraphs.

1) **Multi-exposure imaging using two omnidirectional cameras mounted on an unmanned airship.** Multi-exposure images are captured with multiple shutter speeds using two omnidirectional cameras mounted on the top and bottom faces of an unmanned airship. Since the camera atop the vehicle mainly captures the sun and sky, ND filters are attached to that camera. In addition, shutter speeds are controlled automatically so as to capture multi-exposure images effectively.

2) **HDR image generation from multi-exposure images.** HDR spherical images from two omnidirectional cameras are respectively generated using multi-exposure images. There are misalignments among the multi-exposure

Figure 3. Unmanned airship and omnidirectional cameras. Two cameras are mounted on the top and bottom of the airship. ND filters are attached to the camera on the top. A GPS antenna is also mounted atop the airship.

images caused by the changing position and orientation of the camera. We deal with misalignments due to change in the orientation of the camera, which dominantly affects the amount of misalignment. These are corrected by estimating the change in camera orientation from the captured image sequence.

3) **Combination of HDR images captured by two cameras.** Full spherical HDR images are generated from HDR images from two different cameras. In this study, it is difficult to fix the relative geometric relationship between the cameras, because we use an unmanned airship that has a deformable body. The two HDR images are aligned by estimating the relative rotation between the cameras in every frame. In addition, we correct a chromatic change that occurs in the images captured with ND filters.

B. Multi-exposure imaging using two omnidirectional cameras mounted on an unmanned airship

1) Configuration of the aerial imaging system: A radio controlled unmanned airship that is 12 m long (Fig. 3) is used as the platform for aerial imaging. Spherical image sequences with missing areas are captured using two omnidirectional multi-camera systems (Point Grey Research Ladybug2, see Table I) mounted on the top and bottom of the airship. The cameras are connected to a laptop PC for storing the captured images with time-stamps. ND filters (Fujifilm Corp., ND 2.0) that transmit 1% of the light are attached to the camera on the top of the vehicle as was done in a related study that directly captured the sun and sky [9]. Figs. 1(a) and 1(b) show panoramic images generated by removal of limb darkening and geometric transformation [11]. Note that the amount of limb darkening is different between the images captured with and without ND filters. The airship is also equipped with a differential GPS (Hitachi Zosen Corp., P4-GPS) to acquire the capture positions of the images, which can be used for superimposing virtual objects in augmented telepresence.

2) Automatic control of shutter speeds: The shutter speeds used to capture multi-exposure images are automatically controlled using previous images. Many still cameras provide an auto-bracketing function for capturing multi-exposure images. Those cameras determine one correct exposure from the brightness of the scene, and fixed multiples of the original exposure value are used as the other exposure values [12]. Grossberg and Nayar [13] proposed a method to determine unfixed exposure sets from the dynamic range of the scene. To determine a more appropriate exposure set in our study, an HDR histogram of the previous multi-exposure image sequence is used to reduce the effects of large quantization steps on human vision, such as pseudo-edges due to the small number of multi-exposure images.

New shutter speeds $s_{new_1}, s_{new_2}, ..., s_{new_n}$ are determined by multi-exposure images captured using old shutter speeds $s_{old_1}, s_{old_2}, ..., s_{old_n}$. We use $n = 4$ as the number of shutter speeds because the omnidirectional Ladybug2 cameras used in our experiment have four registers to store the shutter speeds.

The highest shutter speed s_{new_1} is simply determined such that the scene can be captured without saturation from the image captured using s_{old_1}:

$$s_{new_1} = \begin{cases} 0.5 s_{old_1} & (L_{max_1} = 255) \\ \dfrac{255 + \theta_{sh}}{2 L_{max_1}} s_{old_1} & (L_{max_1} \le \theta_{sh}) \\ s_{old_1} & (otherwise), \end{cases} \quad (1)$$

where $L_{max_1}(s_{old_1})$ denotes the maximum intensity in the image captured using s_{old_1}. Further θ_{sh} is a threshold that limits s_{new_1} to $\theta_{sh} < L_{max_1} < 255$ in case the response curve is linear, and $\theta_{sh} = 192$ is used experimentally in Section IV.

When a small number of multi-exposure images are acquired, the effects of large quantization steps, such as pseudo-edges, can appear in the HDR image generated. The other shutter speeds $s_{new_2}, ..., s_{new_n}$ are determined to reduce such effects. To estimate the shutter speeds that have minimum quantization steps, an HDR histogram is calculated from the captured images as illustrated in Fig. 4. $H_{max_i}(s_{new_i})$ is the maximum intensity to capture using the ith highest ($i \ge 2$) shutter speed s_{new_i} in the HDR

TABLE I
SPECIFICATIONS OF LADYBUG2

Item	Specification
Number of cameras	6 (five in horizontal ring, and one on top)
Resolution	1024×768 (for each CCD)
FOV	More than 75% of the full sphere
CCD	Sony ICX204AK
Frame rate	Maximum 30fps
Number of shutter registers	4 (to capture multi-exposure images)

$$\Delta_4 = \frac{H_{max_4}}{255} \qquad \Delta_3 = \frac{H_{max_3}}{255} \qquad \Delta_2 = \frac{H_{max_2}}{255} \qquad \Delta_1 = \frac{H_{max_1}}{255}$$
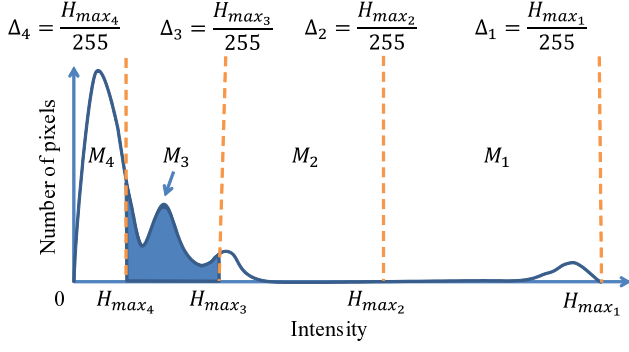
Figure 4. Example of HDR histogram for $n = 4$, where Δ_i denotes quantization steps and H_{max_i} is the maximum intensity that can be captured using shutter speed s_{new_i}. Further, M_3 is the number of pixels in the filled area of the histogram, and the other M_i are determined in a similar fashion.
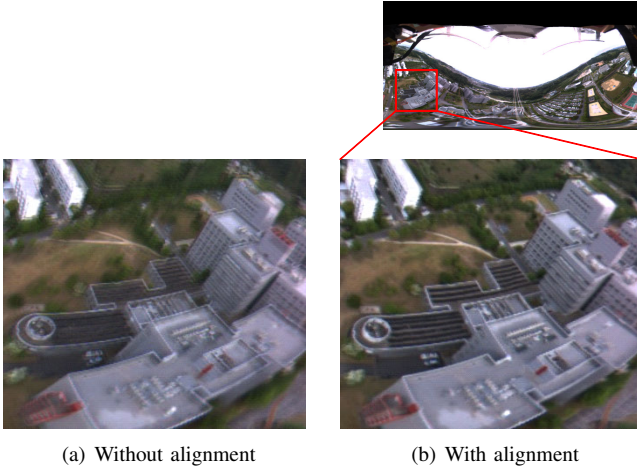

(a) Without alignment   (b) With alignment

Figure 5. HDR images with and without multi-exposure image alignment.

histogram. $M_i(s_{new_i})$ is denoted using $H_{max_i}(s_{new_i})$ as

$$M_i = \sum_{k=\mathcal{H}}^{H_{max_i}} j_k, \qquad (2)$$

where j_k is the number of pixels whose intensity is k, and $\mathcal{H}$ is defined as

$$\mathcal{H} = \begin{cases} 0 & (i = n) \\ H_{max_{i+1}} & (otherwise). \end{cases} \qquad (3)$$

When the response curve of the camera is regarded as linear, the quantization step corresponding to s_{new_i} on the HDR histogram can be calculated as follows:

$$\Delta_i = \frac{H_{max_i}}{255}. \qquad (4)$$

Finally, $s_{new_i}(i \geq 2)$ is determined by minimizing the energy function E_s with respect to changing $s_{new_i}(i \geq 2)$, where E_s is the sum of the products of the quantization step
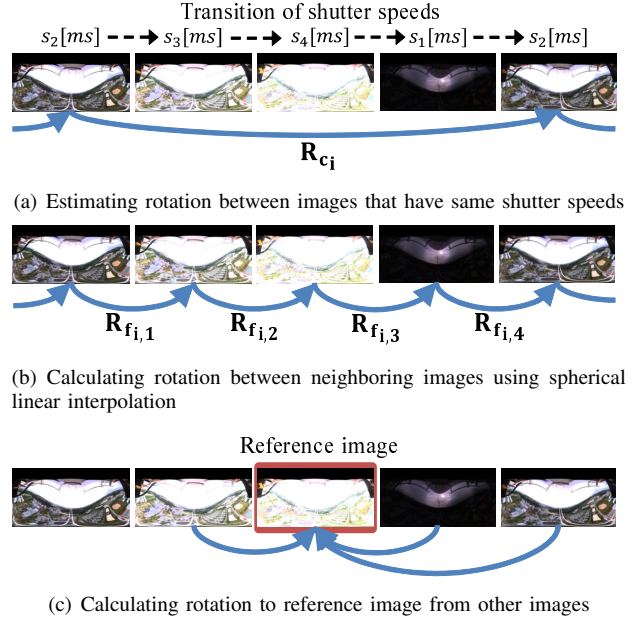

Transition of shutter speeds
$s_2[ms] \dashrightarrow s_3[ms] \dashrightarrow s_4[ms] \dashrightarrow s_1[ms] \dashrightarrow s_2[ms]$

R_{c_i}

(a) Estimating rotation between images that have same shutter speeds

$R_{f_{i,1}} \qquad R_{f_{i,2}} \qquad R_{f_{i,3}} \qquad R_{f_{i,4}}$

(b) Calculating rotation between neighboring images using spherical linear interpolation

Reference image

(c) Calculating rotation to reference image from other images

Figure 6. Process of multi-exposure image alignment.

Δ_i and the number of pixels corresponding to the shutter speed s_{new_i}:

$$E_s = \sum_i (M_i \Delta_i). \qquad (5)$$

E_s is a linear function that has multiple local minimums. We apply a simple coarse-to-fine search technique to find a reasonable solution.

The determination processes of the shutter speeds are repeated every several seconds to allow changes of lighting environment in the real world. Note that s_{new_1} may not converge within a single cycle, and thus several cycles may be needed. Eq. 4 can be changed to apply another nonlinear response curve.

C. HDR image generation from multi-exposure images

1) Alignment of multi-exposure images: There are misalignments among multi-exposure images due to the changing position and orientation of the camera while capturing image sequences. This causes blurring in HDR images generated from misaligned multi-exposure images, as shown in Fig. 5(a).

We assume that the amount of misalignment is dominantly affected by change in the orientation of the camera, since aerial views are mainly taken from a long distance. Accordingly, we correct the misalignments, as shown in Fig. 5(b), by estimating the change in the camera orientation from the captured image sequence.

Fig. 6 shows the steps to align the multi-exposure images. In the first step, two images having the same shutter speeds are selected, and the camera rotation between the

selected images is estimated as shown in Fig. 6(a). Among multi-exposure images, those having the fewest saturated pixels (intensity of 255) and underexposed pixels (intensity of less than 16 in our implementation) are selected. The corresponding points $(\mathbf{p}_m, \mathbf{q}_m)$ between the selected images are determined using the KLT tracker [14] and are projected onto the unit sphere. The parameters for rotation $\mathbf{Rc_i}$ are estimated by nonlinearly minimizing the energy function E_l defined as the sum of squares of the Euclidean distances of the projected corresponding points $|\mathbf{p}_m, \mathbf{q}_m|$:

$$E_l = \sum_m |\mathbf{p}_m, \mathbf{q}_m|^2. \qquad (6)$$

RANSAC is used to reduce errors due to mismatches.

Then, as shown in Fig. 6(b), parameters for rotation between each two adjacent images $\mathbf{Rf_{(i,j)}}$ are calculated by interpolating $\mathbf{Rc_i}$ using spherical linear interpolation.

Parameters for rotations to an arbitrary reference image from neighboring images are calculated from $\mathbf{Rf_{(i,j)}}$ as shown in Fig. 6(c). Multi-exposure images aligned to the reference image are acquired by transformation using parameters for rotation to the reference image. To generate aligned multi-exposure images for a whole video sequence, $\mathbf{Rf_{(i,j)}}$ must first be calculated in a whole sequence, and then each frame in the sequence is used as the reference image.

2) HDR image generation: An HDR imaging method for multi-exposure images proposed by Debevec and Malik [8], which is widely used to capture HDR scenes using LDR cameras, is used to compose intensity in multi-exposure LDR images. In this study, it is necessary to consider light attenuation due to ND filters attached to the camera on the top. If the response curve is linear or linearized in advance, intensities in HDR image I_h are calculated using the LDR intensity I_l, the nominal light transmittance η of the ND filter, and the shutter speed t[s] of the LDR image:

$$I_h = \begin{cases} \gamma \frac{I_l}{t} & \text{(without ND filters)}, \\ \gamma \frac{I_l}{\eta t} & \text{(with ND filters)}. \end{cases} \qquad (7)$$

Although the scale factor γ is meaningless when only the relative pixel intensities are required, it can be determined appropriately to calculate physical absolute radiance values $[\mathrm{W/sr/m^2}]$. The HDR intensities calculated from each set of multi-exposure images are composed in accordance with the method of Debevec and Malik [8].

D. Combination of HDR images captured by two cameras

1) Alignment of HDR images captured by two cameras: The two HDR images captured from the top and bottom of the airship are aligned by estimating the relative rotation between the cameras. To estimate the parameters for rotation, the missing areas in the images captured by the two cameras are manually masked in advance, as shown in the left of Fig. 7. Note that only one mask image is required for each camera over the whole sequence, because the missing area in
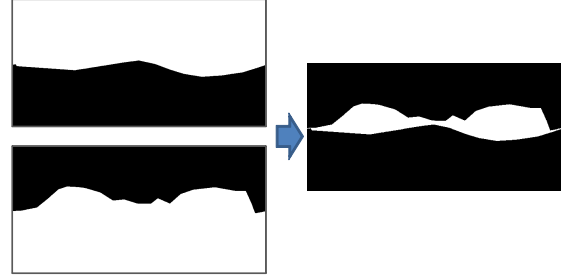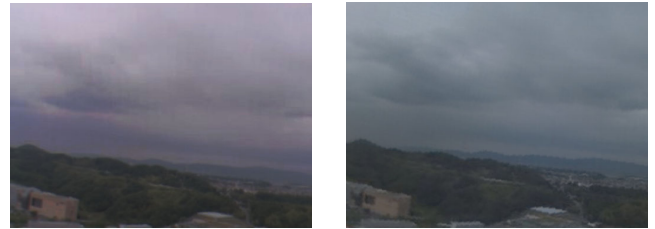

Figure 7. Mask images used for alignment of images from two cameras. Top left: Black pixels indicate a missing area from the top of the airship. Bottom left: Black pixels indicate a missing area from the bottom of the airship. Right: White pixels indicate an overlap area.

(a) Without ND filter (image captured from bottom of airship). Average intensity: $(R, G, B) = (111.5, 108.3, 119.7)$

(b) With ND filter (image captured from top of airship). Average intensity: $(R, G, B) = (95.1, 103.5, 111.9)$

Figure 8. Example of chromatic change due to ND filter. A pair of HDR images converted to the same exposure are shown for a close-up of a part of the overlap areas.

the omnidirectional image does not change significantly. The area displayed as white pixels in the right of Fig. 7 shows the overlap area where the scene can be captured from both cameras without occlusions. This region is defined as the conjunction of negation of the missing areas in each image.

The corresponding points are detected by using the KLT tracker [14] on the feature points in the overlap area in the image captured from the bottom of the airship. The parameters for rotation between the cameras from top to bottom are determined using detected correspondences in the same way as in Section III-C1.

2) Correction of chromatic change due to ND filters : Although ND filters are designed to transmit all wavelengths of light equally, the ND filter actually causes chromatic change [9]. The ND filters used in our experiment transmit less red light, as shown in Fig. 8. The chromatic changes are corrected by estimating linear transformation parameters from intensity in the overlap areas of the images from two cameras. The RGB values $(R_{top}(\mathbf{x}), G_{top}(\mathbf{x}), B_{top}(\mathbf{x}))$ for a pixel $\mathbf{x}$ in the image captured from the top of the airship
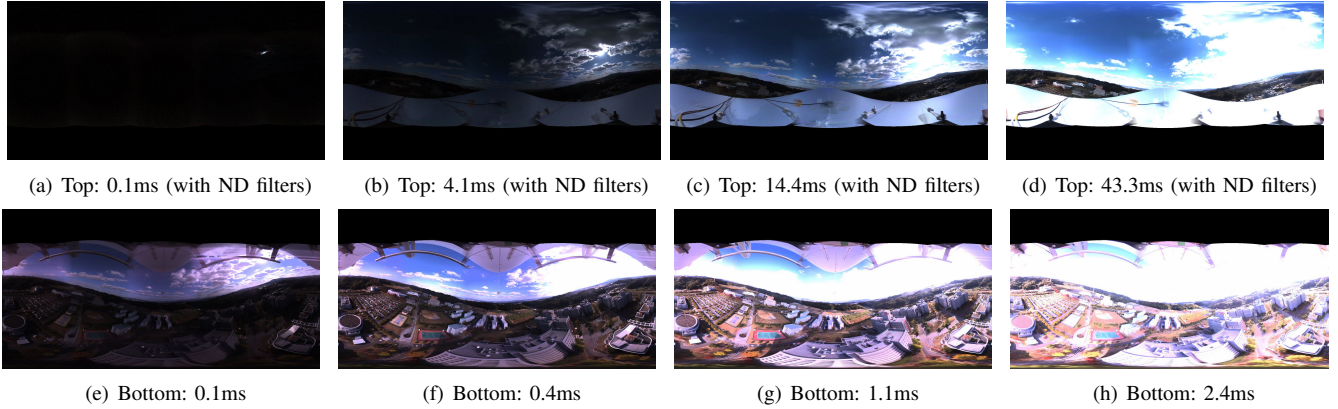
(a) Top: 0.1ms (with ND filters) (b) Top: 4.1ms (with ND filters) (c) Top: 14.4ms (with ND filters) (d) Top: 43.3ms (with ND filters)

(e) Bottom: 0.1ms (f) Bottom: 0.4ms (g) Bottom: 1.1ms (h) Bottom: 2.4ms

Figure 9.   Captured multi-exposure images and corresponding shutter speeds.

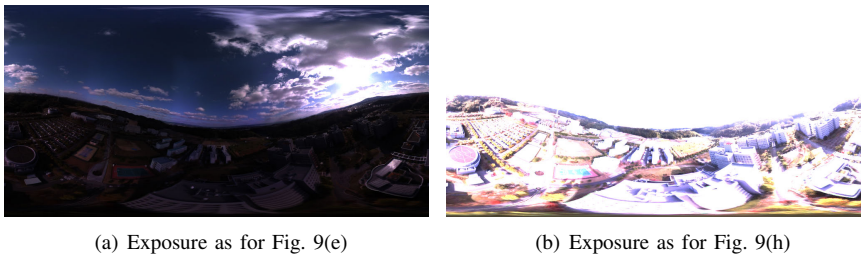(a) Exposure as for Fig. 9(e) (b) Exposure as for Fig. 9(h)

Figure 10.   Full spherical HDR images with cropped intensity and with exposures equal to those of multi-exposure images.

Figure 11.   Full spherical image tone-mapped in accordance with the proposal of Reinhard et al. [15]

are converted by the following linear transformations:

$$R'_{top}(\mathbf{x}) = \beta_r R_{top}(\mathbf{x}), \quad (8)$$
$$G'_{top}(\mathbf{x}) = \beta_g G_{top}(\mathbf{x}), \quad (9)$$
$$B'_{top}(\mathbf{x}) = \beta_b B_{top}(\mathbf{x}), \quad (10)$$

where β_r is estimated by

$$\beta_r = \frac{\Sigma_{\mathbf{x} \in A} \frac{R_{bot}(\mathbf{x})}{R_{top}(\mathbf{x})}}{N_A}. \quad (11)$$

Note that $(R_{bot}(\mathbf{x}), G_{bot}(\mathbf{x}), B_{bot}(\mathbf{x}))$ denote the RGB values of the pixel $\mathbf{x}$ in the image from the bottom of the airship. A denotes the overlap area, and N_A indicates the number of pixels belonging to A. In the same way, β_g and β_b are also estimated.

3) Combination of corrected HDR images from two cameras: Full spherical images are finally generated by combining the pairs of HDR images with alignment and chromatic correction. The intensities in the overlap area in the full spherical image are determined by alpha blending of two images. From the intensities I_{top} and I_{bot} of a pixel in the overlap areas of two cameras, the intensity I_{full} of the corresponding pixel of a full spherical image is calculated as

$$I_{full} = \alpha I_{bot} + (1 - \alpha) I_{top}, \quad (12)$$

where α varies linearly between zero on the upper boundary of the overlap area and unity on the lower boundary.

IV. EXPERIMENTAL RESULTS

A. Experiment using still images

To confirm that the HDR image generated by the proposed method represents the real environment reasonably, we conducted an experiment to generate a full spherical HDR image using still images captured using an unmanned airship above our campus. The airship was at 130 m in altitude and moved at 3 m/s while capturing multi-exposure images. The captured multi-exposure images and corresponding shutter speeds are shown in Fig. 9. Figs. 1(a) and 1(b) show the HDR images from the top and bottom of the airship, respectively. The full spherical HDR image composed using Figs. 1(a) and 1(b) is shown in Fig. 1(c). It is shown that the two images from the top and bottom were combined successfully by the alignment and chromatic correction without any artifacts. Fig. 10 shows the full spherical images visualized with exposures equal to those in Figs. 9(e) and 9(h), respectively. We confirm that the full spherical HDR image reproduces the captured multi-exposure images reasonably. The full spherical HDR image can also be visualized by typical tone-mapping methods such as that proposed by Reinhard et al. [15], as shown in Fig. 11. Tone-mapped full spherical images are suitable for

(a) 1st frame | (b) 100th frame | (c) 200th frame

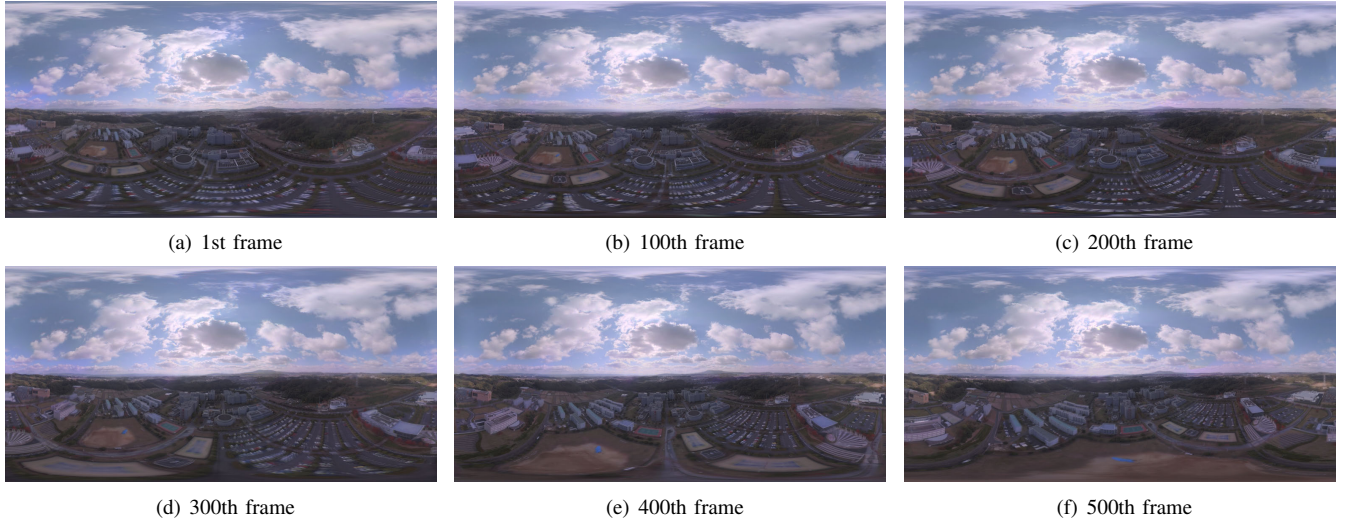(d) 300th frame | (e) 400th frame | (f) 500th frame

Figure 12. Full spherical tone-mapped images generated from video frames. The images were aligned using the estimated camera orientation [16].

immersive telepresence, providing the user with the sense of being able to look around the location, with the specific textures of various radiances.

B. Experiment using video sequence

To generate full spherical HDR videos that can be applied to augmented telepresence, we employed the approach to a video sequence consisting of 500 frames. The airship was at 130 m in altitude and moved at 5–8 m/s while capturing multi-exposure images. The frame rate of the generated HDR video was 16 fps, which is same as that of the source multi-exposure video. The processing time was about 10 s per frame. The position and orientation of the camera on the bottom of the airship were estimated by the structure-from-motion approach for omnidirectional cameras [16], and Fig. 12 shows frames of the full spherical images aligned using camera orientation. The position and orientation of the video frames were successfully estimated. This information can be used for geometric registration between real and virtual objects in augmented telepresence.

C. Discussions about acquirable dynamic range

In the result, several pixels around the sun are still saturated in spite of exploiting the image captured with ND filters using the highest shutter speed $s = 0.1$ ms, which is the smallest value selectable for the camera. In the case of Fig. 9, the dynamic ranges that can be captured without saturation and underexposure are $1 : 2^{8.58}$ for the camera on the bottom of the airship, and $2^{2.47} : 2^{15.23}$ for the camera on the top, when saturation intensity is defined as 255 and underexposure intensity is defined as less than 16. This indicates that the dynamic range of the camera atop the airship is too low to capture the dynamic range of the sky, which can approach $1 : 2^{17}$. In the experiment it is

necessary to use ND filters with less light transmission to capture images without saturation around the sun. To select ND filters, we also have to consider the negative effects on the appearance and the alignment processes due to a growth in underexposed pixels.

V. CONCLUSIONS

This paper focused on an aerial HDR imaging system generating full spherical images without any missing areas. The full spherical HDR images generated can be applied to telepresence, IBL, augmented telepresence, and other applications using omnidirectional images. Multi-exposure images used to generate HDR images are captured by a pair of omnidirectional cameras mounted on the top and bottom of an airship, which is the platform for aerial imaging. In experiments, full spherical HDR images were successfully generated from image sequences captured from the sky above our campus. It has also been confirmed that a full spherical HDR video can be generated with the position and orientation information of the camera for applying to augmented telepresence. In future work, we will use full spherical HDR images for augmented telepresence by IBL approaches using information on camera position and orientation.

REFERENCES

[1] J. Steuer, "Defining virtual reality: Dimensions determining telepresence," *Journal of Communication*, vol. 42, no. 4, pp. 73–93, 1992.

[2] P. Debevec, "Rendering synthetic objects into real scenes: Bridging traditional and image-based graphics with global illumination and high dynamic range photography," in *Proc. ACM SIGGRAPH '98*, Orlando, FL, 1998, pp. 189–198.

[3] F. Okura, M. Kanbara, and N. Yokoya, "Fly-through Heijo palace site: augmented telepresence using aerial omnidirectional videos," in *Proc. ACM SIGGRAPH'11 Posters*, Vancouver, BC, 2011, p. 78.

[4] D. Anguelov, C. Dulong, D. Filip, C. Frueh, S. Lafon, R. Lyon, A. Ogale, L. Vincent, and J. Weaver, "Google street view: Capturing the world at street level," *IEEE Computer*, vol. 43, no. 6, pp. 32–38, 2010.

[5] R. Azuma, Y. Baillot, R. Behringer, S. Feiner, S. Julier, and B. MacIntyre, "Recent advances in augmented reality," *IEEE Computer Graphics and Applications*, vol. 21, no. 6, pp. 34–47, 2001.

[6] N. Kawai, T. Sato, and N. Yokoya, "Image inpainting considering brightness change and spatial locality of textures and its evaluation," in *Proc. Pacific-Rim Symp. on Image and Video Technology (PSIVT'09)*, Tokyo, 2009, pp. 271–282.

[7] N. Kawai, K. Machikita, T. Sato, and N. Yokoya, "Video completion for generating omnidirectional video without invisible areas," *IPSJ Trans. on Computer Vision and Applications*, vol. 2, pp. 200–213, 2010.

[8] P. Debevec and J. Malik, "Recovering high dynamic range radiance maps from photographs," in *Proc. ACM SIGGRAPH'97*, Los Angeles, CA, 1997, pp. 369–378.

[9] J. Stumpfel, C. Tchou, A. Jones, T. Hawkins, A. Wenger, and P. Debevec, "Direct HDR capture of the sun and sky," in *Proc. Int'l Conf. on Computer Graphics, Virtual Reality, Visualisation and Interaction in Africa (AFRIGRAPH'04)*, Stellenbosch, 2004, pp. 145–149.

[10] E. Reinhard, G. Ward, S. Pattanaik, P. Debevec, W. Heidrich, and K. Myszkowski, *High dynamic range imaging: Acquisition, display, and image-based lighting*. Morgan Kaufmann, 2010.

[11] S. Ikeda, T. Sato, and N. Yokoya, "High-resolution panoramic movie generation from video streams acquired by an omnidirectional multi-camera system," in *Proc. IEEE Int'l Conf. on Multisensor Fusion and Integration for Intelligent System (MFI'03)*, Tokyo, 2003, pp. 155–160.

[12] S. Kang, M. Uyttendaele, S. Winder, and R. Szeliski, "High dynamic range video," in *Proc. ACM SIGGRAPH'03*, San Diego, CA, 2003, pp. 319–325.

[13] M. Grossberg and S. Nayar, "High dynamic range from multiple images: Which exposures to combine?" in *Proc. ICCV Workshop on Color and Photometric Methods in Computer Vision (CPMCV)*, Nice, 2003.

[14] J. Shi and C. Tomasi, "Good features to track," in *Proc. IEEE Computer Society Conf. on Computer Vision and Pattern Recognition (CVPR'94)*, Seattle, WA, 1994, pp. 593–600.

[15] E. Reinhard, M. Stark, P. Shirley, and J. Ferwerda, "Photographic tone reproduction for digital images," in *Proc. ACM SIGGRAPH'02*, San Antonio, TX, 2002, pp. 267–276.

[16] T. Sato, S. Ikeda, and N. Yokoya, "Extrinsic camera parameter recovery from multiple image sequences captured by an omnidirectional multi-camera system," in *Proc. European Conf. on Computer Vision (ECCV'04)*, vol. 2, Prague, 2004, pp. 326–340.